Effects of Er and Zr additions on the as-cast microstructure and on the solution heat treatment response of innovative Al-Si-Mg-based alloys

M. Colombo* [1], R. H. Buzolin[2], E. Gariboldi[1], L. Rovatti[1], R. Vallant[2], C. Sommitsch[2]
[1] Politecnico di Milano, Dipartimento di Meccanica, via Giuseppe la Masa, 1, Milano, Italy
[2] Graz University of Technology, Institute of Materials Science, Joining and Forming, Graz, Austria

Corresponding author's email: marco1.colombo@polimi.it

Abstract: The microstructure of Al-Si-Mg alloys strongly depends on their chemical composition and on the heat treatment that is performed during production. The influence of solution heat treatment and the additions of Er and Zr on the microstructure of gravity cast A356 (Al-7Si-0.4Mg) are investigated. The as-cast microstructure is characterized by means of grain size measurements, morphology of eutectic Si as well as morphology, area fraction and chemical composition of the intermetallic compounds. The morphology of eutectic Si is found to be unstable with respect to high temperature exposure during solution heat treatment. The evolution mechanisms are described using thermodynamic and kinetic models for the investigated alloys and validated using optical and SEM micrographs. The effects of high temperature exposure during solution heat treatment on the amount and morphology of the intermetallic compounds is also characterized using optical and SEM micrographs.

1 Introduction:

Because of a combination of excellent castability, which allows to obtain components with complex shape, and satisfactory mechanical properties, Al-Si-Mg cast alloys are widespread in many industrial fields [1].

The microstructure features of this family of Al alloy in the as-cast state strongly depend on the casting technology (specifically on the solidification rate) and on the chemical composition of the alloy [2-6]. In casting techniques with a relatively low solidification rate, such as low pressure die casting, eutectic Si exhibits a plate-like morphology in the absence of modifying element such as Sr or Na [1]. In this case, the eutectic Si act as stress concentrator reducing the ductility of the alloy.

In the case of A356 alloy (Al-7Si-0.4Mg), several classes of intermetallic compounds form during solidification, such as β-Al_5FeSi plates, Chinese script π- $Al_8Mg_3FeSi_6$ and β-Mg_2Si [7-10]. The first two families of intermetallic compounds are due to the presence of Fe as impurity in Al-Si alloys. Those intermetallic compounds have notable influences on the mechanical properties of A356 alloy. β-Al_5FeSi plates cause a reduction in ductility of the alloy because of their particular elongated shape as well as they notable brittleness. Moreover, the β-Al_5FeSi plates promote the formation of micro- and macro-porosity in interdendritic regions during solidification [7-9].

Solution Heat Treatment (SHT) at 813 K for 5 h is usually performed on gravity cast A356 alloy. The microstructure modification caused by SHT affects positively the mechanical properties of Al-Si-Mg cast alloys, as it is shown in literature [11-15]. Among the microstructure transformation phenomena that occur during SHT, the morphological modification of eutectic Si and the partial or complete dissolution of primary intermetallic compounds are the most relevant.

The plate-like morphology of the eutectic Si is not stable at high temperatures [16-18]. During SHT the Si particles progressively fragment and evolve until a final stage where a spheroidal morphology is reached due to Gibbs free energy minimization [19].

The dissolution of intermetallic compounds increases the concentration of alloying elements in the matrix and allows the formation of precipitates during subsequent aging, enhancing the mechanical strength of the material. Not all the intermetallic compounds dissolve during SHT of A356: Al_5FeSi plates are partially spheroidized instead of completely dissolving [20]; β-Mg_2Si, on the other hand dissolve during SHT increasing the Si and Mg content in the matrix, enhancing the precipitation strengthening during aging [20, 21]. The effects of SHT on π-$Al_8Mg_3FeSi_6$ are unclear. It is reported that either the $Al_8Mg_3FeSi_6$ totally dissolve during SHT, or Mg present in the intermetallic compounds is selectively released in solid solution, resulting in the formation of fine, Fe-rich intermetallic compounds [20].

The addition of other alloying elements in Al-Si-Mg cast alloys modifies their microstructure features, inducing the formation of different types of intermetallic compounds [5, 6, 22, 23] as well as modifying the morphology of eutectic Si [24-26]. In this regard, the addition of Er and Zr to the commercial A356 alloy show enhanced room and high temperature mechanical properties due to microstructure modification [27, 28]. However, the kinetics of spheroidization of the eutectic Si and the evolution of the formed intermetallic compounds during SHT in the modified A356 alloys containing Er and Zr have not been investigated. This paper aims to describe those processes using thermodynamic and kinetic models, providing a better understating of the role of Er and Zr additions on the modification of the as-cast microstructure of an A356 alloy.

2 Materials and Methods

Al-15 wt% Er and Al-10 wt% Zr master alloys were added to a commercial A356 alloy to obtain the chemical composition reported in table 1.

Table. 1: Chemical composition (wt.%) of the investigated alloys, measured using Glow Discharge Optical Emission Spectroscopy (GDOES).

	Si	Mg	Fe	Ti	B	Er	Zr	Al
A356	7.02	0.41	0.07	0.14	0.0001	-	-	bal.
E3	7.38	0.36	0.08	0.14	0.0001	0.29	-	bal.
EZ35	6.85	0.38	0.09	0.12	0.0003	0.26	0.59	bal.

The reference and master alloys were melted in an induction furnace at a temperature of 1073 K under protective atmosphere of Ar. Magnetic stirring was used to mix the melt, minimizing inhomogeneities in the chemical composition. The melt was then poured into a stainless-steel mould preheated at 473 K. The cast ingots were cylinders of ~40 mm in diameter and ~ 120 mm in height.

Cuboidal samples with dimensions of ~ 10x10x10 mm^3 were cut from the central part of the cast ingots, in equivalent positions for all the studied alloys and oriented randomly with respect to the ingot axis, and subjected to SHT at 813 K for different holding times (from 5 min to 5 h). Central regions of the ingots were selected because have the minimum solidification rate and thus more effectively simulate the microstructure of industrial casting.

Specimens for microstructure investigations were prepared using a standard metallographic route: grinding using abrasive SiC-based papers followed by polishing using 3 and 1 μm diamond pastes, and finally polishing using colloidal silica suspension (0.04 μm abrasive size).

Solidification rate in the area of the ingots used in the present investigation was estimated to be ~ 2°C/s [27, 28], according to the empirical equation relating Secondary Dendrites Arm Spacing (SDAS) to the solidification rate reported in equation 1 [29].

$$SDAS = 39.4R^{-0.317} \quad (1)$$

where SDAS represents the distance between the axis of secondary dendrites arms (measured to be 31.5 ± 2.5 μm) and R is the solidification rate (measured in °C/s).
The equation was obtained for the same alloy, cast in an equivalent ingot and at the same casting temperature.
Polished samples were utilized to investigate the microstructure features of the as-cast and solution heat treated alloys using optical microscopy. A minimum of five representative optical micrographs were taken and the morphology of eutectic Si for different holding times during solution heat treatment at 813 K was quantitatively characterized. For quantitative analysis of the microstructure a minimum of 1500 eutectic Si particles were measured in each condition. Each eutectic Si particle present in the micrographs was approximated as an ellipse. The major axis, minor axis and aspect ratio (defined as the ratio between the major and minor axes) were measured using ImageJ software. The measured data from the analysis of the evolution of the eutectic Si during SHT at 813 K was utilized in kinetic and thermodynamic models to describe the globularization behavior of the investigated alloys.
Measurements of the area fraction of intermetallic compounds in the as-cast condition and after 5 h SHT were performed by using a minimum of five representative random SEM-BSE (backscattered electron detector in Scanning Electron Microscope) micrographs and analyzed using ImageJ software. The as-cast samples utilized for grain size measurements were chemically etched after metallographic preparation using a solution of 75 ml HCl + 20ml HNO_3 + 5ml HF for an immersion time of 30 s. Grain size was measured using the linear intercept method for at least five representative optical micrographs acquired using polarized light.
In order to qualitatively investigate the 3D morphology evolution of eutectic Si and to confirm the kinetic and thermodynamic models presented, samples subjected to different SHT times (5 min, 2 and 5 h) were deep selective etched in 15 vol.% HCl aqueous solution at room temperature for 20 min and analyzed by means of SEM. The deep etched samples were also analyzed using SEM to describe qualitatively in 3D the evolution of the morphology and distribution of the intermetallic compounds during SHT. Because of the small size of some types of intermetallic compounds, their location in the eutectic region and possibly particle undermining during etching, it was not always possible to investigate in detail all types of intermetallic compounds in deep etched samples.

3 Results

3.1 As-cast microstructure

The as-cast microstructures of the investigated alloys are shown in Figure 1. They are formed by primary α-Al dendrites, surrounded by eutectic Si and different types of intermetallic compounds. The types of intermetallic compounds varied according to the chemical composition of the alloy. Globular dendrites are observed in EZ35 alloy, figure 1c), while elongated dendrites are visible for the other two alloys, figure 1a) and b).
The plate-like morphology of eutectic Si is highlighted in the high magnification optical micrographs shown in figure 1d). The typical morphology of the modified Si due to Er and Zr additions is visible for E3 and EZ35 in figures 1e) and 1f), respectively.

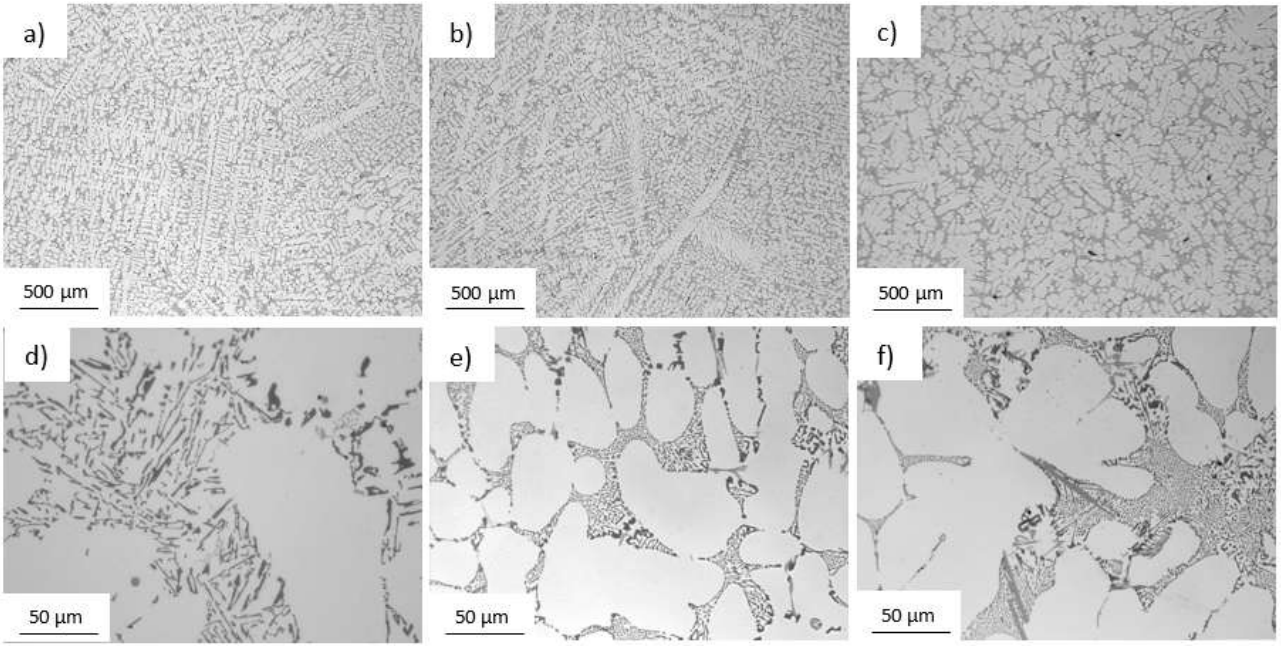

Figure 1: Representative optical micrographs of the as-cast microstructure of a), d) A356, b), e) E3 and c), f) EZ35.

Representative low-magnification optical micrographs are shown in figure 2. The average grain size is 1462 ± 350 µm, 1157 ± 186 µm and 383 ± 98 µm for A356, E3 and EZ35, respectively.

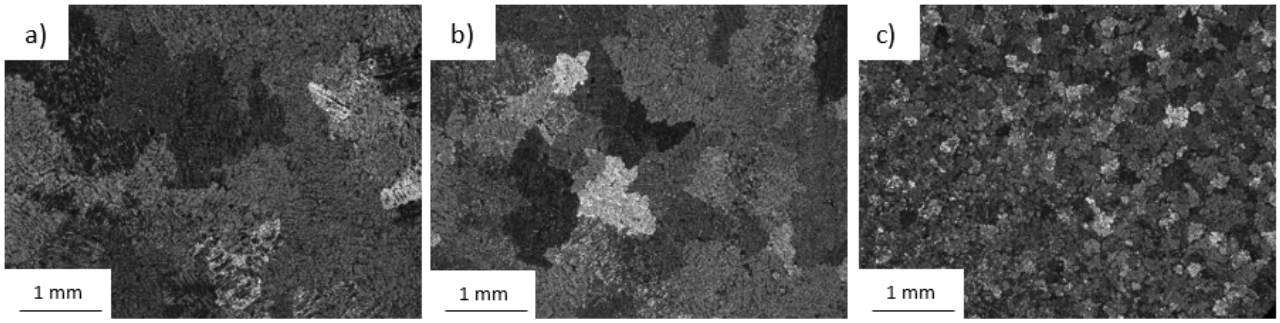

Figure 2: Typical optical micrographs of the as-cast of a) A356, b) E3 and c) EZ35 alloys. Polarized light was utilized to obtain the grain contrast.

SEM micrographs of the as-cast alloys after deep etching are shown in Figure 3. The morphology of eutectic Si is qualitatively observed and the plate-like morphology of eutectic Si in A356 is shown in figures 3a) and 3d). On the other hand, the eutectic Si exhibits a coral-like fibrous shape for the E3 and EZ35 alloys, as shown in figures 3b) and 3e) for E3 and in figure 3c) and 3f) for EZ35.
The insert in figure 3d) highlights the edges of growing steps of eutectic Si, while the inserts in figures 3e) and f) show particles protruding from eutectic Si, with a size ranging from ~ 300 nm to ~ 1 µm. The chemical composition of the protruding particles was measured using Energy Dispersive X-Ray Spectroscopy (EDXS) and reported in table 2.

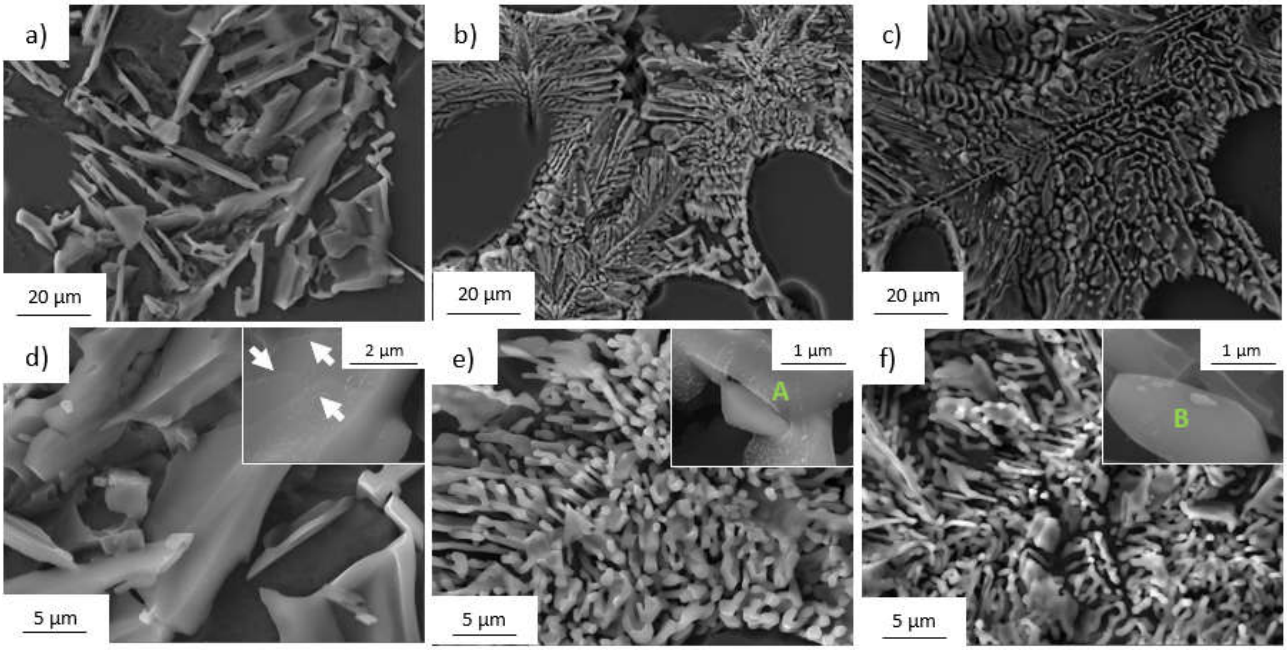

Figure 3: Typical SEM-SE (secondary electron) micrographs of the deep-etched eutectic Si for the as-cast: a), d) A356, b), e) E3 and c), e) EZ35. Insert in figure 3d) highlights the growing steps of eutectic Si; inserts in figures e) and f) highlight particles protruding from eutectic Si.

Table 2: Results of Energy Dispersive X-Ray Spectroscopy (EDXS) analyses (at.%) of intermetallic compounds particles shown in the inserts of figure 3e) and 3f).

	Al	Si	Er	Zr
A	39.2	51.1	9.7	-
B	40.1	50.9	8.4	0.6

Representative BSE micrographs of the as-cast A356, E3 and EZ35 are shown in figure 4. and the typical intermetallic compounds present in the investigated as-cast alloys are highlighted. SEM micrographs and EDXS analyses of the intermetallic compounds present in the A356 alloy show the presence of π ($Al_8Mg_3FeSi_6$) and Mg_2Si, figure 4a), in agreement with the literature [21].

The alloys modified with additions of Er and Zr exhibited different microstructural features. Er and Zr promote the formation of different intermetallic compounds. Figures 4b) and c) show the typical intermetallic compounds formed in the E3, and figures 4d), e) and f) in the EZ35.

For the E3 alloy the addition of ~0.3 wt.% Er induces the formation of three different types of intermetallic compounds: a blocky shape Mg-rich intermetallic compound (C in figure 4b), plate-like particles with a Fe/Er at. % ratio of ~ 1.2 (D in figure 4c) and a complex shape intermetallic compound with a Fe/Er ratio of ~ 4.7 (E in figure 4c). It appears that the addition of Er to A356 hinders the formation of the typical intermetallic compounds found in Al-Si-Mg alloys.

For the EZ35, the addition of 0.59 wt.% Zr induces the formation of small particles at the plates' intersection and plate-like intermetallic compounds that may act as inoculants during solidification for the α-Al dendrites (G and F in figure 4d, respectively). The intermetallic compounds found in the E3 alloy were also observed in the EZ35 alloy: the plate-like particles with Fe/Er ratio of ~ 1.2 (H in figure 4d), the blocky shape Mg-rich intermetallic compounds (I in figure 4e) and the complex shaped precipitates with a Fe:Er ratio of ~ 5.6 (L in figure 4f). Moreover, similar morphology of those intermetallic compounds in comparison to E3 is observed. A slight enrichment in Zr in their composition is found, though.

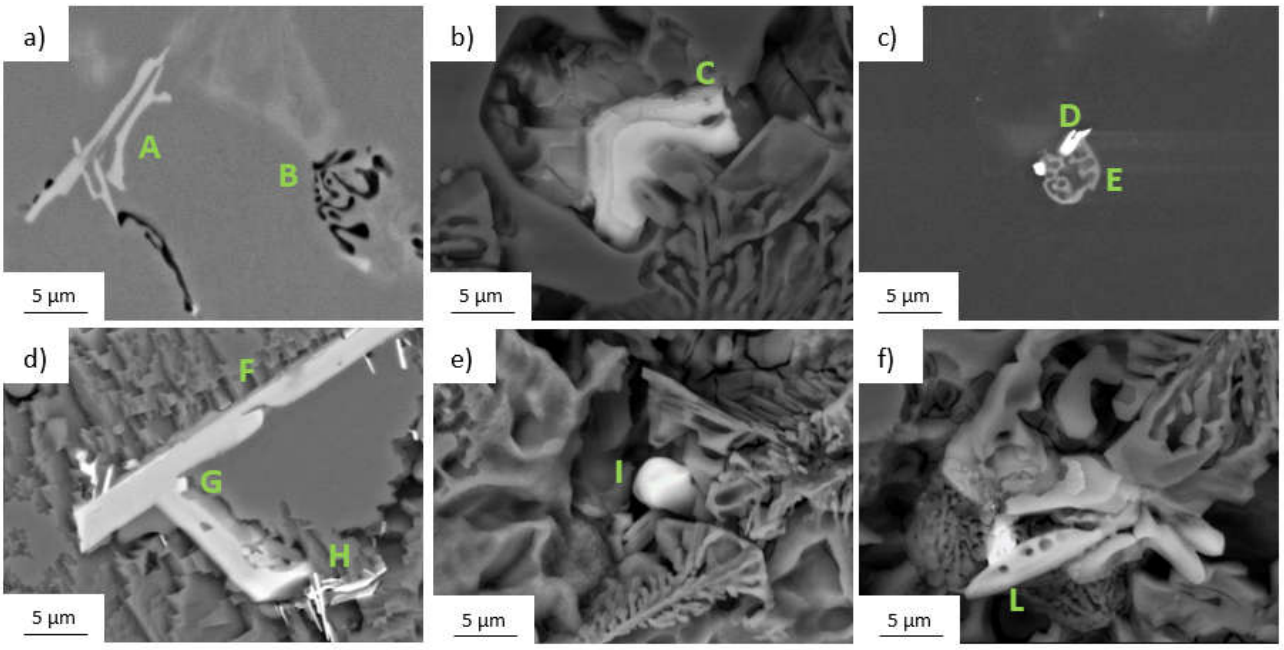

Figure 4: Typical intermetallic compounds present in the as-cast a) A356, b) and c) E3 and d) e) and f) EZ35.

Results of EDXS analyses on the intermetallic compounds shown in figure 4 are exhibited in table 3. Due to the fact that the EDXS probe has a finite analysis volume, the chemical composition of intermetallic compounds may be affected by surrounding regions and should be considered qualitatively.

The area fraction of intermetallic compounds in the as-cast state is shown in table 4 for the investigated alloys.

Table 3: Results of EDXS analyses (at.%) of the intermetallic compounds present in the as-cast A356, E3 and EZ35 alloys and shown in figure 4.

	Al	Si	Mg	Fe	Ti	Er	Zr
A	70.0	17.9	9.3	2.8	-	-	-
B	84.5	9.6	5.9	-	-	-	-
C	69.5	20.7	6.2	-	-	3.6	-
D	46.0	31.9	1.0	11.3	-	9.8	-
E	50.7	26.2	10.5	10.4	-	2.2	-
F	67. 4	10.2	0.6	0.5	12.5	0.8	8.0
G	75.6	11.5	1.3	1.9	0.2	8.1	1.4
H	43.9	37.9	1.1	8.8	0.2	7.1	1.0
I	51.1	34.4	8.2	1.2	-	3.8	1.3
L	46.9	33.5	2.4	13.5	-	2.4	1.3

Table 4: Area fraction (%) of intermetallic compounds for the as-cast investigated alloys. Values for EZ35 include intermetallic compounds found in the inner regions of dendrites (which account for 0.2%).

	A356	E3	EZ35
Area fraction of intermetallic compounds	0.5 ± 0.1	0.9 ± 0.1	1.3 ± 0. 2

205
206 *3.2 Microstructure evolution during SHT*
207
208 Grain coarsening did not occur after 5 h SHT for the investigated alloys. The deep etched samples
209 after SHT at 813 K were utilized to investigate qualitatively the effects of SHT on the morphology of
210 eutectic Si. Non-deep etched samples were utilized to perform quantitative measurements of the
211 eutectic Si morphology. Representative SEM micrographs obtained from deep etched specimens after
212 5 min SHT are shown in figure 5. 5 min SHT is not sufficient to promote significant morphological
213 changes in eutectic Si for the investigated alloys. Nevertheless, two phenomena can be observed in
214 A356, namely the formation of cavities inside Si plates, as shown in figure 5a) and the rounding of
215 plates borders (figure 5d). Similarly, in regions were the eutectic Si shows less pronounced fibrous
216 morphology, the formation of cavities is observed for E3 and EZ35, as shown in figure 5b) and 5e)
217 for E3 and in figure 5c) and 5f) for EZ35.
218

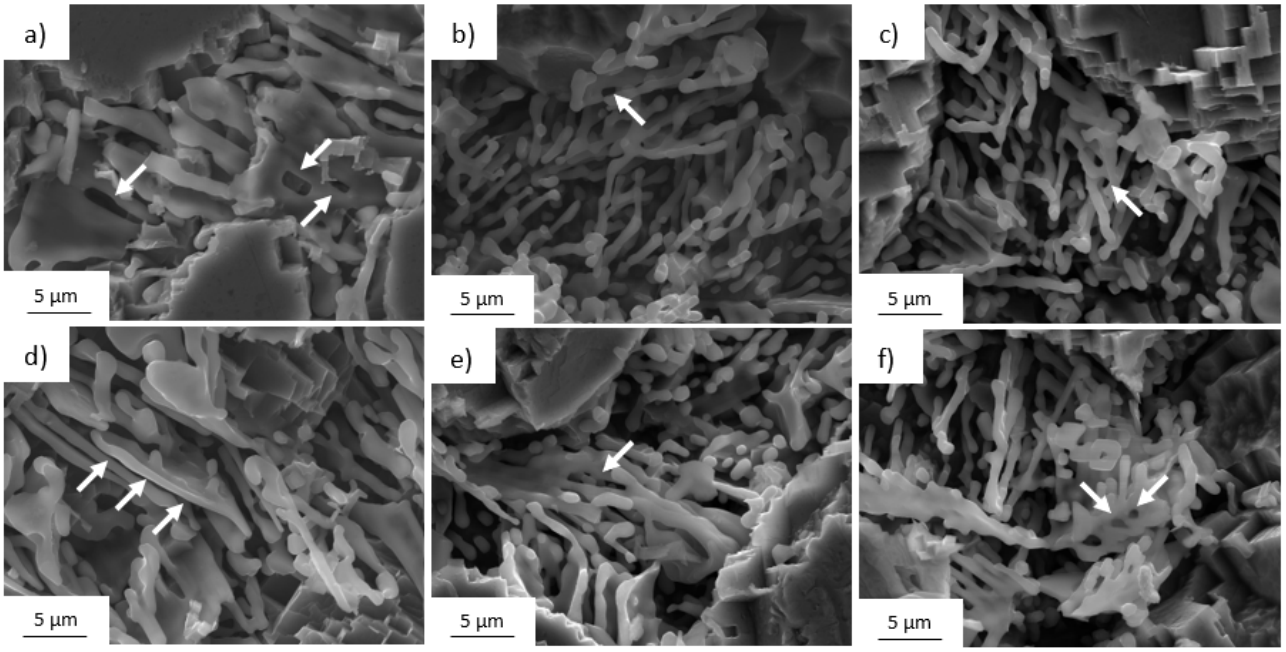

219
220
221 **Figure 5:** SEM-SE (secondary electrons) micrographs of deep-etched samples showing the
222 morphology of eutectic Si after 5 min SHT at 813 K for the a) and d) A356, b) and e) E3 and c) and
223 f) EZ35.
224
225 After 2 h SHT at 813 K a complete breakage of Si plates is observed for the A356, figure 6a). On the
226 other hand, for the E3 and EZ35 alloys the breakage of eutectic branches is partial and local thinning
227 of eutectic Si is observed.
228

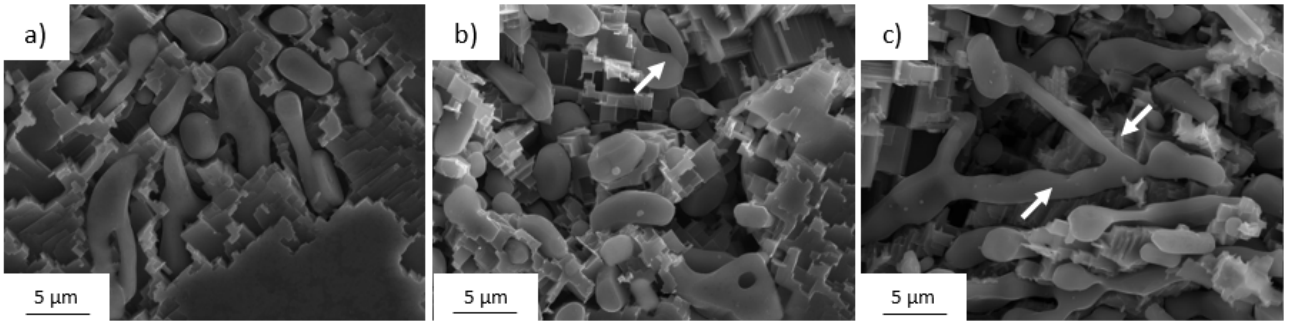

229
230

Figure 6: SEM-SE (secondary electrons) micrographs showing the deep-etched morphology of eutectic Si after 2 h SHT at 813 K for the a) A356, b) E3 and c) EZ35.

After 5 h SHT at 813 K significant modifications of the morphology of eutectic Si are observed, figure 7. Discrete Si particles are formed in all investigated alloys. The eutectic Si exhibits a more complex shape in A356 compared to the E3 and EZ35 alloys. Er-containing particles protruding from Si after 5 h SHT are observed for the E3 and EZ35 alloys and highlighted in the inserts of figures 7b) and 7c).

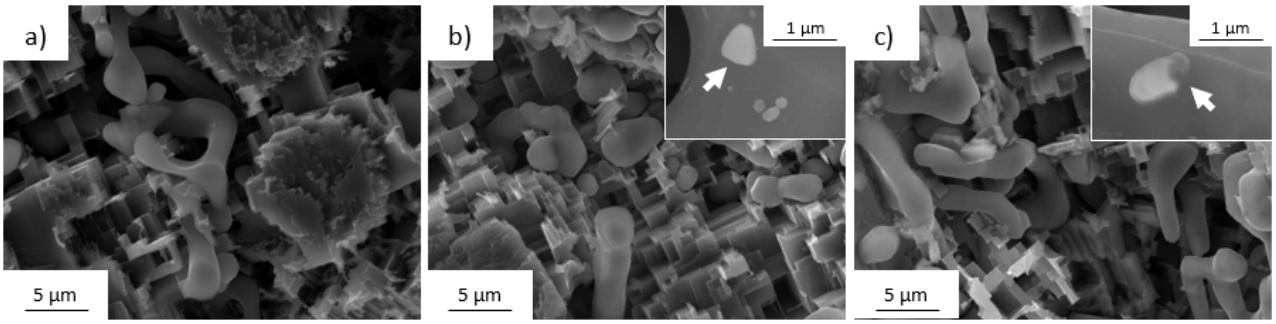

Figure 7: SEM-SE (secondary electrons) micrographs showing the deep-etched morphology of eutectic Si after 5 h SHT at 813 K for the a) A356, b) E3 and c) EZ35. A detailed view of the intermetallic compounds protruding from the Si eutectic is shown in the inserts in b) and c).

The evolution of the morphology of the eutectic Si during SHT at 813 K was quantified by measuring eutectic geometric features using optical micrographs obtained after different SHT times. Figure 8 shows the evolution of Si aspect ratio and average length as a function of SHT time.

Notable changes after SHT in the morphology of eutectic Si for the A356 alloy are observed. The aspect ratio varies from 10.8 ± 2.5 for the as-cast A356 to 4.2 ± 1.2 after 5 h SHT. The length of the eutectic Si monotonically decreases from 27.2 ± 3.8 µm in the as-cast condition, to 9.2 ± 1.8 µm after 5 h SHT.

For the modified alloys with Er and Zr, the morphology of the Si eutectic is not significantly affected by SHT in comparison to the A356 alloy. The aspect ratio varies from 1.6 ± 0.5 in the cast condition to 1.2 ± 0.2 for E3 after 5 h SHT for E3 alloys. For the EZ35 alloy, it varies from 1.7 ± 0.3 in the cast condition to 1.3 ± 0.2 for EZ35 after 5 h SHT. The length of the eutectic Si is slightly affected by the SHT for alloy E3, exhibiting a value of 3.5 ± 0.6 µm in the as-cast condition and 4.5 ± 0.7 µm after 5 h SHT. For the EZ35, it varies from 2.3 ± 0.6 µm for the as-cast condition to 4.0 ± 0.3 µm after 5 h SHT.

260

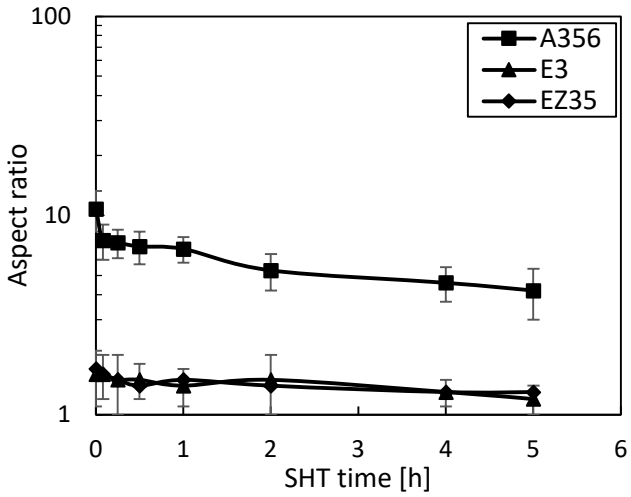
100
10
1
Aspect ratio
0
1
2
3
4
5
6
SHT time [h]
A356
E3
EZ35

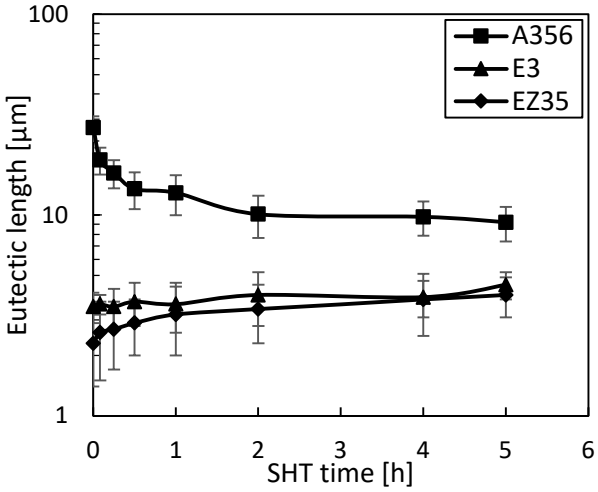
100
10
1
Eutectic length [µm]
0
1
2
3
4
5
6
SHT time [h]
A356
E3
EZ35

261

262

Figure 8: Evolution of geometric features of eutectic Si in the investigated alloys as a function of the SHT time.

Concerning the evolution of the intermetallic compounds during SHT, small Fe containing intermetallics are observed in the A356 alloy after 5h SHT at 813 K (figure 9). The EDXS point analysis of these Fe containing particles is shown table 5.

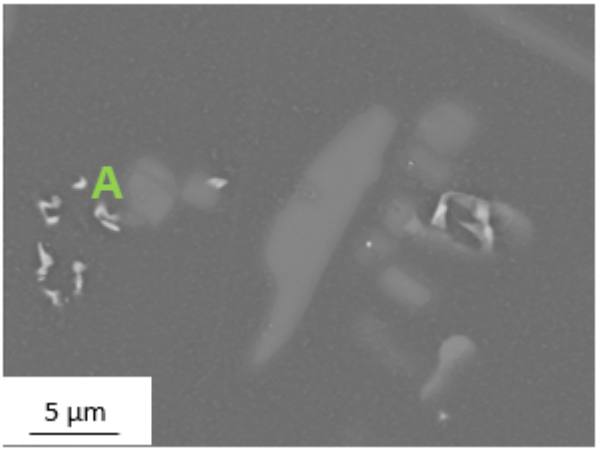

Figure 9: Typical SEM-BSE (backscattered electron) micrograph showing the intermetallic compounds present in the A356 after 5 h SHT at 813 K.

Table 5: Results of EDXS analysis on intermetallic compound A shown in figure 9. Values are in at.%.

	Al	Si	Mg	Fe
A	73.1	16.6	2.7	7.6

The three types of intermetallic compounds that are observed for the as-cast E3 alloy, are also observed in the microstructure of the E3 after 5 h SHT at 813 K: continuous intermetallic compounds (A in figure 10a), plate-like intermetallic compound characterized by a length approximately ranging from 5 to 15 µm (B in figure 10a) and complex shaped particles (C in figure 10b). Intermetallic compound A is the only one with significant content of Er and Mg and low content of Fe, as shown in the EDXS analyses in table 6. On the other hand, the other two types of intermetallic compounds exhibit different Fe/Er wt.% ratios: ~ 1.2 for intermetallic compound B and ~ 4.2 for intermetallic compound C.

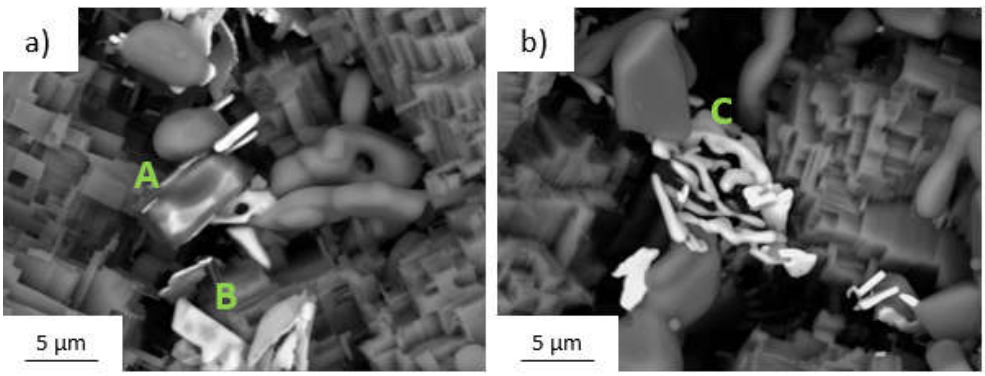

Figure 10: SEM-BSE (backscattered electron) micrographs of deep etched specimen showing the morphology of the different types of intermetallic compounds present in E3 alloy after 5 h SHT at 813 K. a) shows plate-like and blocky-shaped intermetallic compounds, b) shows complex-shaped particles.

Table 6: Results of EDXS point analyses for the intermetallic compounds shown in figure 10. Values are in at.%.

	Al	Si	Mg	Fe	Er
A	61.4	30.4	3.2	0.3	4.7
B	46.7	29.8	0.7	12.3	10.5
C	60.4	24.7	0.6	11.5	2.8

The different types of intermetallic compounds found in the as-cast EZ35 alloy are also observed after 5 h SHT at 813 K, figure 11. One type of intermetallic compound is observed in the center of the dendrites (highlighted with A in figure 11a). In this region smaller particles are also observed at the interface between the intermetallic compound and the α-Al matrix, B. The other types of intermetallic compounds are located in the interdendritic region (C, D and E in figure 11b). The addition of Zr does not induce notable modifications in the morphology of the intermetallic compounds present in the interdendritic regions of EZ35 alloy. Slight variations of their chemical composition are observed, though, as reported in table 7.

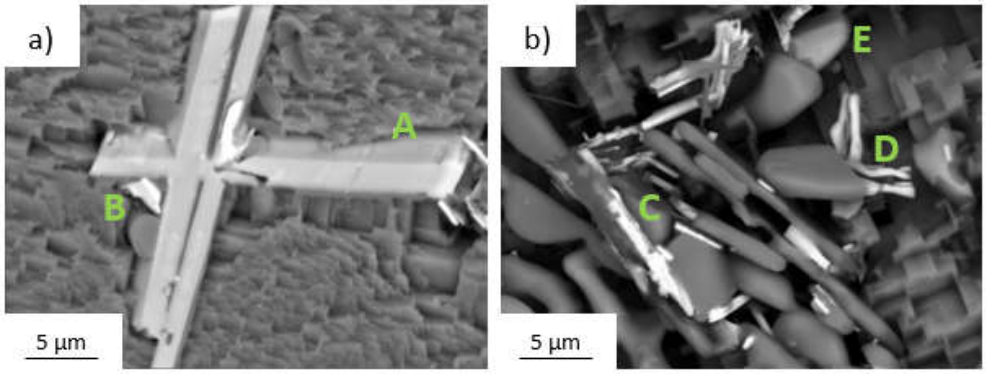

Figure 11: SEM-BSE (backscattered electron) micrographs of deep etched specimen showing the morphology of the different types of intermetallic compounds in EZ35 after 5 h SHT at 813 K. a) shows intermetallic compounds in the central region of dendrites, b) representative particles in eutectic regions.

The area fraction of intermetallic compounds for the investigated alloys after 5 h SHT at 813 K is shown in table 8.

Table 7: Results of EDXS point analyses for the intermetallic compounds shown in figure 11. Values are in at.%.

	Al	Si	Mg	Fe	Ti	Er	Zr
A	67.4	10.2	0.6	0.6	12.5	0.8	7.9
B	78.5	10.6	0.6	0.3	0.2	9.3	0.5
C	33.5	47.1	1.1	8.8	0.2	7.0	2.3
D	24.1	60.3	0.3	11.1	-	2.0	2.2
E	65.9	17.8	5.8	0.1	-	8.4	2.0

Table 8: Area fraction (%) of intermetallic compounds found in the investigated alloys after 5 h SHT. Values for EZ35 include intermetallic compounds in the inner regions of dendrites (which account for 0.19%).

	A356	E3	EZ35
Area fraction of intermetallic compounds	0.3 ± 0.1	0.6 ± 0.1	1.1 ± 0.2

4 Discussion

4.1 As cast microstructure

The as-cast microstructure of the A356 alloy was modified with the additions of Er and Zr. Notable differences in the dendritic morphology are observed. The EZ35 alloy exhibited the most pronounced microstructure change. While the A356 and the E3 exhibited a typical elongated dendritic morphology, globular grains are observed for the EZ35 alloy. The inoculation effect of $(Al, Si)_3(Zr, Ti)$ pro-peritectic intermetallic compounds that were formed during solidification in the EZ35 alloy is attributed as the reason for the refined globular microstructure of EZ35 alloy [28]. The grain size was refined with addition of 0.59 wt.% Zr to the Al-Si-Mg system, figure 2. The grain size decreases from an average value of 1462 µm for alloy A356 to 383 µm for EZ35.The grain nucleation efficacy of Zr-containing particles is maximized by the low concentration of B in the EZ35 alloy, table 1. In presence of B and Ti, inoculation occurs due to TiB_2 particles which, as demonstrated recently by HRTEM investigations, are decorated by a layer of Al_3Ti [30, 31]. Zr additions prevent the formation of the Al_3Ti layer, inducing the precipitation of a ZrB_2 monolayer. This causes a lattice parameter expansion of the boride and a consequent reduction in its nucleation effectiveness [30, 35]. The low amount of B present in the investigated alloys is not sufficient to promote the precipitation of TiB_2 particles (an effective inoculation due to B-containing particles is achieved for a B concentration of ~200 ppm [33]), minimizing the poisoning action of Zr.

It is reasonable that $(Al, Si)_3(Zr, Ti)$ particles are the same phase as $(Al, Si)_3Zr$, since Ti concentration is only slightly higher compared to its maximum solubility in Al at the peritectic temperature (0.1 wt.% at 937 K, as reported in [34]) and undergo partial substitution of Zr atoms with Ti atoms.

No literature is available regarding the lattice parameter of $(Al, Si)_3(Zr, Ti)$, which plays the major role as effective inoculant. Nevertheless, investigations about $(Al, Si)_3Ti$ and $Al_3(Ti, Zr)$ particles show that Si and Ti substitutions slightly reduce the lattice parameter of Al_3Ti and Al_3Zr, respectively [35, 36], potentially indicating an improved inoculation efficacy for $(Al, Si)_3(Zr, Ti)$. Further investigations are required to confirm this hypothesis.

The morphology of eutectic Si was also notably modified with additions of Er and Zr to A356 alloy. The eutectic Si exhibited an elongated plate shape for the A356 alloy, while nearly spherical particles are observed for the modified alloys (figures 1d), 1e) and 1f)). This finding is in agreement with the literature [27, 28]. The SEM micrographs of deep etched as-cast alloys (figure 3) allow qualitative characterization of the morphology of eutectic Si. The typical plate-like morphology observed in Al-Si-Mg cast alloys [24, 37, 38] is also observed for the A356 alloy, figures 3a) and d). In this case, eutectic Si grows in a strongly anisotropic manner, preferably along <211> crystallographic directions [25, 37, 39]. The growth rate, on the other hand, is found to be minimum along the direction perpendicular to the (111) plane [25, 37, 39], leading to the plate-like appearance observed in figures 3a) and d). A schematic representation of the Si growth is shown in figure 12. Step growth fronts are also observed in the SEM micrographs and highlighted by dashed lines in the insert of figure 3d). A more comprehensive discussion about Si growth in unmodified Al-Si alloys is out of the scope of the present paper, but can be found in the literature [25, 37, 39].

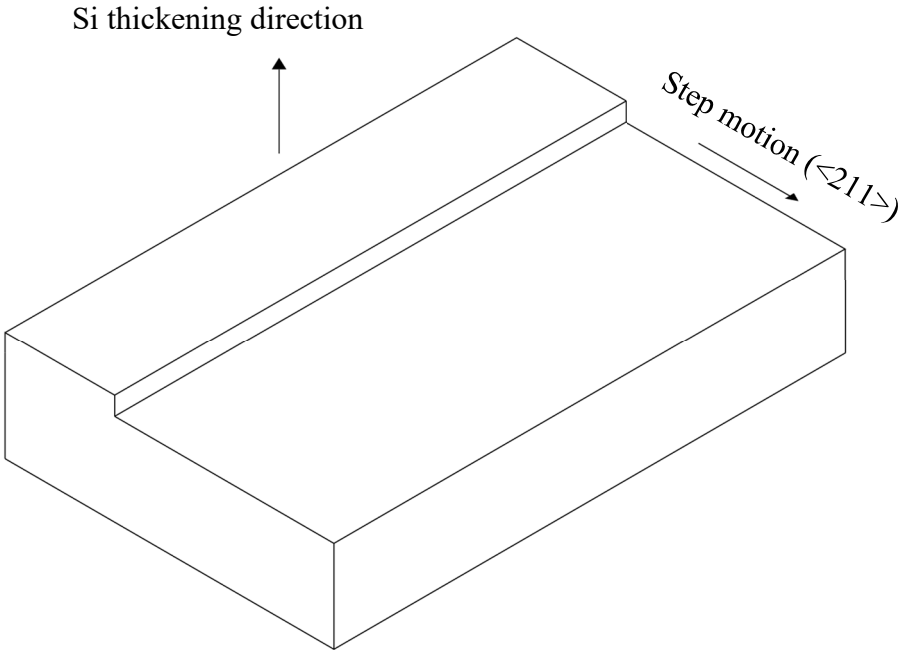

Figure 12: Schematic representation of the growth of eutectic Si in unmodified Al-Si cast alloys.

The E3 and EZ35 alloys exhibit a coral-like eutectic Si, typical of alloys in which modifying elements such as Sr, Na, Yb and Eu are added [25, 26, 39, 40] or when fast cooling during solidification is achieved [41]. The casting parameters were kept constant for the production of the investigated alloys. No differences between the eutectic Si of E3 and EZ35 are observed. Therefore, the addition or Er to the Al-Si-Mg system modified the morphology of the eutectic Si. Moreover, Zr does not play any role on the modification of the morphology of eutectic Si. The inserts in figures 3e) and 3f) show the presence of Er-containing particles in the vicinity of eutectic Si, similarly to what was found for Al alloys containing Yb and Eu [26, 40]. These particles are formed by solute entrapment of the modifying element during eutectic solidification [40].

Two typical intermetallic compounds are observed in Al-Si-Mg cast alloys: π-Chinese script and Mg_2Si particles. The very limited concentration of Fe in the alloys is not sufficient to promote significant formation of β (Al_5FeSi) plates, which are not observed in the microstructure of the alloy, in agreement with the literature [10].

The phase identification for the Al-Si-Mg alloys containing Er and Zr is rather complex because of the absence of a complete phase diagram for the investigated systems. Nevertheless, similarities can be found between the types of intermetallic compounds found in the as-cast E3 and the EZ35 alloys, with a slight Zr enrichment for those found in the EZ35 alloy.

4.2 Microstructural evolution during SHT

Plate-like microstructural constituents can undergo several morphological changes when exposed to high temperatures, namely direct cylinderization, boundary splitting and edge spheroidization [17]. Among these phenomena, the typical ones for high aspect ratio plates play the most important role in the modification of the plate-like eutectic Si:

i) boundary splitting: it induces the formation of grooves on longitudinal defects by surface diffusion of atoms away from the forming groove and, finally, leads to the plate breaking into cylinders;

ii) edge spheroidization: it is triggered by the formation of ridges at the plate terminations, due to surface diffusion of atoms away from the plate border. The formed ridges

are not stable at high temperature, because of their finite radius of curvature [42], resulting in ridges breaking and formation of small spheroids at the periphery of Si plates. This mechanism is particularly relevant for plates with relatively lower aspect ratio.

Morphological modifications are observed in the eutectic Si of the investigated alloys after 5 min SHT at 813 K. For the A356 alloy, the Si plates exhibit shape instability. The two instability mechanisms described above are concurrently acting: boundary splitting, highlighted by arrows in figure 3a) and edge recession with consequent formation of ridges, indicated by the arrows in figure 3d). For the E3 and EZ35 alloys, similar phenomena are observed in locally non-modified Si particles (figures 3b) and 3d) for E3, and figures 3c) and 3f) for EZ35).

The eutectic Si in as-cast A356 alloy is characterized by high aspect ratio and by the presence of internal defects (e.g. twins and step edges highlighted by dashed lines in the insert of figure 3d). These features facilitate boundary splitting, which is found to be the dominant instability mechanism for this alloy (figure 6a) and 7a)).

The formula shown in equation 2 is used to model the time needed for breakage of the plates of eutectic Si to be completed [18].

$$\tau = \frac{0.0335 t^3 kT}{(1-\sin\varphi) D c_0 \gamma_s \Omega} \quad (2)$$

Where t is the eutectic Si plate thickness, k is the Boltzmann's constant, T is the absolute temperature at which the process occurs, c_0 is the equilibrium solubility of the plate component in the matrix phase (in at.%), D is the diffusion coefficient of the plate component in the matrix, **Ω** is the atomic volume of the plate component, φ is half of the dihedral angle at the boundary juncture and γ_s is the surface energy of the Si-matrix interface (figure 13). The values used for the mentioned parameters are reported in table 9.

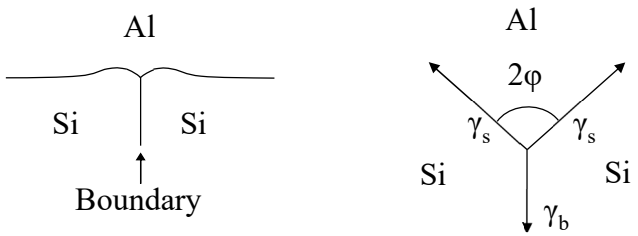

Figure 13: a) schematic representation of a boundary grooving, b) schematic vectorial representation of the surface energies at a triple point.

Table 9: Values of the parameters used for the calculation of the breaking time for the eutectic Si plate in the A356 alloy.

Quantity	Meaning	Value	Source
t	Si plate thickness	2.5 10^{-6} m	This work
k	Boltzmann's constant	1.38 10^{-23} J/K	
T	SHT temperature	813 K	This work

φ	Half dihedral angle at the defect juncture	129.5 °	[43]
D	Si diffusion coefficient in Al at the SHT temperature	3.99 10^{-13} m^2/s	[44]
Ω	Si atomic volume	5.74 10^{-30} m^3	
c_0	Si concentration in Al at the SHT temperature	1.2 at.%	[45]
γ_s	Surface energy at the Si-Al interface	1 J/m^2	[19]

The calculated time for breakage of the eutectic Si plates (τ) is 154 min for the A356 alloy. The deep etched A356 specimens subjected to 2 h SHT at 813 K shows that plate breaking by boundary splitting is completed after 2 h SHT, figure 5a).

2 h SHT was also performed for the modified alloys and the results are shown in figure 6b) and 6c) for alloy E3 and alloy EZ35, respectively. Surface perturbation and partial fragmentation of eutectic Si for E3 and EZ35 alloys is achieved after the 2 h SHT and it is visible when figures 3 and 5 are compared to figure 6.

The fragmentation process of eutectic Si in modified alloys can be described as a consequence of the intrinsic thermodynamic instability of thin cylinders with respect to longitudinal variations of their radius and is termed Plateau-Rayleigh instability [42]. Perturbations present at the Si surface are amplified by surface diffusion of atoms from regions with higher surface energy (concave regions) to regions with lower surface energy (convex regions), finally leading to the rupture of coral branches. A schematic representation of the mechanism underlying Si branches fragmentation process, together with the most important geometric parameters for the process modelling, is shown in figure 14.

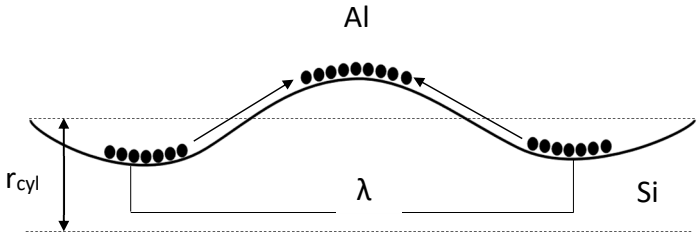

Figure 14: Schematic representation of the perturbation evolution in eutectic Si during SHT by surface diffusion of Si atoms. r_{cyl} represents the radius of the unperturbed Si and λ the perturbation wavelength.

The perturbations descending from Rayleigh instability can propagate only if a critical perturbation wavelength, λ_{crit}, is reached. This critical perturbation can be correlated to the radius of the unperturbed cylinder according to equation 3 [17]:

$$\lambda_{crit} = 2\pi\sqrt{2}r_{cyl} \quad 3)$$

Where r_{cyl} is the unperturbed cylinder radius [19]. Using the values shown in table 5 for r_{cyl} equation 3 yields a λ_{crit} value of 15.55 μm for E3 and 10.22 μm for EZ35. Approximating the perturbed rods and the fragmented particles as perfect cylinders and spheres and assuming that the volume is conserved during the fragmentation process, the radius of the fragmented spherical particles is calculated to be 3.3 μm and 2.16 μm for E3 and EZ35, respectively.

Fragmentation kinetics of eutectic Si in a Sr-modified A356 alloy was modelled in literature by applying the Johnson-Mehl-Avrami-Kolmogorov (JMAK) equation, described in equation 4:

$$f_{frag} = 1 - exp\left(-k_{frag} t^n\right) \quad (4)$$

Where k_{frag} and n are the fragmentation kinetic parameter and the time exponent, considered as 1.73 10^{-3} s^{-1} and 1, respectively, for a Sr-modified A356 subjected to a SHT at 813 K [46].
Longer SHT times cause coarsening of the fragmented eutectic Si particles. Assuming a volume-controlled coarsening process, the temporal evolution of the eutectic Si radius can be described using equation 5:

$$\frac{dr}{dt} = \frac{k_{coars}}{r^2} \quad (5)$$

Where r is the instantaneous radius of the spherical eutectic Si particle, t is the coarsening time and k_{coars} is a rate constant, that is considered as 7.86 10^{-5} s^{-1}, calculated for a Sr-modified A356 alloy subjected to SHT at 813 K [46].
Modelling the coarsening process requires the definition of an initial radius for the Si spheres (r_0) and an initial coarsening time (t_0, defined as the time when $r = r_0$).
A reasonable value for time at the beginning of the coarsening (t_0) is considered as the time for half of the total volume of eutectic Si to be fragmented (i.e. $f_{frag} = 0.5$) [46]. Using equation 4 a value of 400.6 s is obtained for t_0.
r_0 can be considered as the radius of Si particles immediately after fragmentation, which can be obtained using the thermodynamic considerations on Rayleigh instability (3.3 µm and 2.16 µm for the E3 and EZ35, respectively).
Integrating equation 5 and using the abovementioned initial conditions, equation 5 yields a diameter of Si particles after 5 h SHT at 813 K of 6.68 µm for the E3 alloy and 4.84 µm for the EZ35 alloy.
The calculated diameters are higher compared to the experimentally measured (4.5 and 4.0 for E3 and EZ35, respectively), figure 8. The addition of Er and Zr to the A356 alloy modified the fragmentation and the coarsening kinetics of the eutectic Si, reducing the velocity of the involved phenomena. Further investigation is required to explain the discrepancies between the experimental and modelled values.
The quantitative analyses of the spheroidization of eutectic Si in alloy A356 is shown in figure 8 and 5 h SHT at 813 K is not sufficient to promote complete spheroidization, since the aspect ratio of the eutectic Si particles is approximately 4.2. On the other hand, the average aspect ratio of eutectic Si in the E3 and EZ35 alloys barely varies with the holding time at time and it is close to unity, indicating that shorter SHT at 813 K time is sufficient to promote an almost complete eutectic spheroidization for the modified alloys.
The intermetallic compounds present after SHT at 813 K in the three alloys are reported in figures 9, 10 and 11 for A356, E3 and EZ35, respectively. Mg_2Si particles, found in the as-cast state for A356, are completely dissolved during SHT, confirming literature findings [10]. SEM micrographs shown in figure 9, coupled with the relevant EDXS analyses, suggest that π intermetallic compounds do not dissolve completely during SHT, but rather undergo a compositional change, with a reduction in Mg content and a concurrent relative increase of Fe. This can be observed by the comparison of table 3 and table 5. The SHT at 813 K induces the formation of fine Fe-rich particles for the A356 alloy, shown in figure 9 and similar to those reported in literature [10].
The types of intermetallic compounds found in the as-cast E3 and EZ35 alloys are not dissolved during SHT at 813 K. Nevertheless, differences in the chemical composition of the intermetallic compounds are found for the different holding times. Mg-rich particles undergo selective dissolution. A depletion of Mg is observed during SHT, as suggested by the comparison of their chemical composition before and after SHT (C in table 3 and A in table 6 for E3 and I in table 3 and E in table 7 for EZ35). Similar behavior is observed for the other types of intermetallic compounds present in the modified alloys, as Mg content is lower after SHT at 813 K.

The area fraction of intermetallic compounds decreases after SHT at 813 K for the investigated alloys as a consequence of their lower fraction in equilibrium at 813 K. A notable decrease of the area fraction of intermetallic compounds is found for the A356 alloy (from 0.52% in the as-cast condition to 0.25% after 5 h SHT at 813 K). A complete dissolution of Mg_2Si particles and the selective Mg migration in solid solution from π intermetallic compounds, inducing the formation of small Fe-rich particles, are observed for the A356 alloy solution heat treated at 813 K for 5 h. A decrease of 35% in area fraction of the intermetallic compounds is also observed for the E3 alloy. The lower dissolution of intermetallic compounds for the E3 in comparison to the A356 is attributed to the smaller diffusion coefficient of Er in Al in comparison to Mg in Al. The calculated diffusion coefficient of Er in Al is 4.71×10^{-17} m^2/s, while Mg in Al is 5.17×10^{-13} m^2/s at 813 K [48, 49]. In this way, lower dissolution kinetics is expected for intermetallic compounds containing Er compared to intermetallic compounds containing only Mg. Moreover, the lower solid-state solubility of Er with respect to Mg in Al at 813 K prevents the dissolution of the intermetallic compound containing Er [47], contributing to lower dissolution of the intermetallic compounds for the E3 in comparison to A356. The area fraction of intermetallic compounds in EZ35 is nearly constant for the investigated holding times for SHT at 813 K. The low diffusivity of the alloying elements in Al, as well as the low solubility in Al at the solid state explain the negligible dissolution of intermetallic compounds during SHT for EZ35 [50]. The calculated diffusion coefficient of Zr in Al at 813 K is 2.06×10^{-17} m^2/s [51], while the diffusion coefficient for Mg, Si and Fe are 5.17×10^{-13}, 5.17×10^{-13} and 6.14×10^{-15} m^2/s respectively [48, 52, 53].

5. Conclusions:

From the experimental work presented in this paper the following conclusions are made:

1. Coarse and elongated dendritic structures are observed for A356 and E3, while fine and globular α-Al dendrites are observed for EZ35.
2. Plate-like eutectic Si is found in the microstructure of as-cast A356, while a coral-like shape of the eutectic Si is found in the microstructure of the modified alloys.
3. π-$Al_8Mg_3FeSi_6$ and β-Mg_2Si intermetallic compounds were observed in the as-cast microstructure of A356. A negligible amount of β-Al_5FeSi is observed.
4. Several families of intermetallic compounds were found in the as-cast microstructure of as-cast E3 and EZ35 alloys, both in eutectic regions and in the central part of the dendrites. For E3 alloy blocky shaped Mg-rich particles, plate-like intermetallic compounds with low Fe/Er ratio and complex-shaped phases with high Fe/Er ratio are found; additions of Zr slightly modify the chemical composition of the abovementioned intermetallic compounds and induce the formation of Zr-rich phases in the central regions of Al dendrites.
5. Morphological evolution of eutectic Si during SHT for A356 alloy can be described by boundary splitting, with an average breaking time for Si plates of 2 h.
6. The breakage of the cylindrical eutectic Si during SHT in modified alloys is attributed to Rayleigh instability.
7. SHT at 813 K promotes partial dissolution and modification of the morphology of intermetallic compounds in A356 alloy.
8. Intermetallic compounds in modified alloys are only slightly affected by SHT, both in morphology and chemical composition.

6. References

[1] I. Polmear, Light Alloys: from Traditional Alloys to Nanocrystals, Butterworth-Heinemann, 2005.
[2] K. T. Kashyap, S. Murali, K. S. Raman & K. S. S. Murthy, Materials Science and Technology, 1993, 9, 189-204.
[3] R. Chen, Y. Shio, Y. Xub, C. Liu, Transactions of Nonferrous Metals Society of China, 2014, 24, 1645-1652.

[4] K.T.Akhil, S. Arul, R. Sellamuthu, Procedia Materials Science, 2014, 5, 362-368.
[5] Q. G. Wang, Metallurgical and Materials Transactions A 2003, 34, 2887–2899.
[6] L. Y. Zhang, Y. H. Jiang, Z. Ma, S. F. Shan, Y. Z. Jia, C. Z. Fan, W. K. Wang, Journal of Materials Processing Technology, 2008, 207, 107-111.
[7] M.A. Moustafa, Journal of Materials Processing Technology, 2009, 209, 605-610.
[8] C. Do Lee, Materials Science and Engineering A 2007, 464, 249-254.
[9] C.H. Càceres, Scripta Metallurgica et Materialia, 1995, 32, 1851-1856.
[10] Q. G. Wang, C. J. Davidson, 2001, 36, 739–750.
[11] M. Zhu, Z. Jian, G. Yang, Y. Zhou, Materals and Design, 2012, 36, 243-249.
[12] E. Sjölander, S. Seifeddine, Journal of Materials Processing Technology, 2010, 210, 1249-1259.
[13] F.H Samuel, Journal of Materials Science, 1998, 33, 2283–2297.
[14] M. A. Moustafa, F. H. Samuel, H. W. Doty, Journal of Materials Science, 2003, 38, 4507–4522.
[15] Standard Practice for Heat Treatment of Aluminum-Alloy Castings from All Processes, ASTM Standards.
[16] G. Sharma, r. V. Ramanujan, G. P. Tiwari, Acta Materialia, 2000, 48, 875-889.
[17] J. C. M. Kampe, T. H. Courtney, Y. Leng, Acta Metallurgica, 1989, 37, 1735-1745.
[18] T. H. Courtney, J. C. M. Kampe, Acta Metallurgica, 1989, 37, 1747-1758.
[19] E. Ogris, A. Wahlen, H. Luechinger, P.J. Uggowitzer, Journal of Light Metals, 2002, 2 263–269.
[20] J.A. Taylor, D.H. St John, J. Barresi, M.J. Couper, Materials Science Forum, 2000, 331, 277–282.
[21] P. A. Rometsch, L. Arnberg, D. L. Zhang, International Journal of Cast Metals Research, 2016, 12, 1-8
[22] J. Hernandez-Sandoval, G.H. Garza-Elizondo, A.M. Samuel, S. Valtiierra, F.H. Samuel, Materials and Design, 2014, 58, 89–101.
[23] Y.-C. Tsai, C.-Y. Chou, S.-L. Lee, C.-K. Lin, J.-C. Lin, S.W. Lim, Journal of Alloys and Compounds, 2009, 487, 157-162.
[24] A.K. Dahle, K. Nogita, S.D. McDonald, C. Dinnis, L. Lu, Materials Science and Engineering A, 2005, 413–414, 243–248.
[25] A. Mazahery, M. O. Shabani, Journal of Materials, 2014, 66, 726-738.
[26] J.H. Li, X.D. Wang, T.H. Ludwig, Y. Tsunekawa, L. Arnberg, J. Z. Jiang, P. Schumacher, Acta Materialia, 2015, 84, 153–163.
[27] M. Colombo, E. Gariboldi, A. Morri, Journal of Alloys and Compounds, 2017, 708, 1234-1244.
[28] M. Colombo, E. Gariboldi, A. Morri, Materials Science and Engineering A, 2018, 713, 151-160.
[29] L. Ceschini, A. Morri, A. Morri, A. Gamberini, S. Messieri, Materials and Design, 2009, 30, 4525–4531.
[30] Z. Fan, Y. Wang, Y. Zhang, T. Qin, X.R. Zhou, G.E. Thompson, T. Pennycook, T. Hashimoto, Acta Materialia, 2015, 84, 292–304.
[31] P. Schumacher, A. L. Greer, Materials Science and Engineering, A, 1994, 178, 309-313.
[32] Y. Wang, L. Zhou, Z. Fan, Light Metals, TMS (The Minerals, Metals & Materials Society), 2016, 725-729.
[33] Z. Chen, H. Kang, G. Fan, J. Li, Y. Lu, J. Jie, Y. Zhang, T. Li, X. Jian, T. Wang, Acta Materialia, 2016, 120, 168-178.
[34] H. Okamoto, Journal of Phase Equilibria, 1993, 14, 120-121.
[35] P. S. Mohanty, J. E. Gruzleski, Acta Materialia, 1996, 44, 3749-3760.
[36] M.V. Karpets, Y.V. Milman, O.M. Barabash, N.P. Korzhova, O.N. Senkov, D.B. Miracle, T.N. Legkaya, I.V. Voskoboynik, Intermetallics, 2003, 11, 241–249.
[37] S. Nafisi, R. Ghomashchi, H. Vali, Materials Characterization, 2008, 59, 1466-1473.
[38] A.K. Dahle, K. Nogita, J.W. Zindel, S.D. Mcdonald, and L.M. Hogan, Metallurgical and Materials Transactions A, 2001, 32, 949-960.
[39] M.M. Makhlouf, H.V. Guthy, Journal of Light Metals, 2001, 1, 199–218.
[40] J.H. Li, M. Albu, F. Hofer, P. Schumacher, Acta Materialia, 2015, 83, 187–202.

[41] T. Hosch, R.E. Napolitano, Materials Science and Engineering A, 2010, 528, 226–232.
[42] H. P. Stuewe, O. Kolednik, Acta Metallurgica, 1988, 36, 1705-1708.
[43] H. V. Guthy, Evolution of the Eutectic Microstructure in Chemically Modified and Unmodified Aluminum Silicon Alloys, Worcester Polytechnic Institute (2002).
[44] S. Fujikawa, K. Hirano, Y. Fukushima, Metallurgical Transactions A, 1974, 9, 1811-1815.
[45] J. L. Murray, A. J. McAlister, Bulletin of Alloy Phase Diagrams, 1984, 5, 74-84.
[46] L. J. Colley, M. A. Wells, W. J. Poole, Canadian Metallurgical Quarterly, 2014, 53, 125.137.
[47] H. Okamoto, Journal of Phase Equilibria and Diffusion, 2011, 32, 261-262.
[48] Y. Zhang, K. Gao, S. Wen, H. Huang, Z. Nie, D. Zhou, Journal of Alloys and Compounds, 2014, 610, 27–34.
[49] S.J. Rothman, N. L. Peterson, L. J. Nowicki, L.C. Robinson, Phys. stat. sol. (b), 1974, 9, 29-33.
[50] H. Okamoto, Journal of Phase Equilibria, 2002, 23, 455-456.
[51] K. Hirano, S. Fujikawa, Journal of Nuclear Materials, 1978, 69, 564-566.
[52] S. Fujikawa, K. Hirano, Y. Fukushima, Metallurgical Transactions A, 1978, 9, 1811-1815.
[53] S. Mantl, W. Petry, K. Schroeder, and G. Vogl, Physical Review B, 1983, 27, 5313-5331.